Source Model of the 2014 M_w 6.9 Yutian Earthquake at the Southwestern End of the Altyn Tagh Fault in Tibet Estimated from Satellite Images

Xing Li[1], Wenbin Xu[*2,3], Sigurjón Jónsson[1], Yann Klinger[4], and Guohong Zhang[5]

Abstract

Multiple fault segments ruptured during the 2014 Yutian earthquake, but the detailed source parameters and the mechanism of rupture complexity remain poorly understood. Here, we use high-resolution TanDEM-X satellite data and Satellite Pour l'Observation de la Terre-6/7 images to map the coseismic ground deformation field of the event. We find that the majority of coseismic slip occurred in the upper 10 km with the maximum left-lateral fault slip of ∼2.5 m at ∼6 km depth. The fault ruptured across a large 4.5 km extensional stepover from one left-lateral fault segment to another, with some right-lateral relay faulting in between. We find that the earthquake was followed by shallow afterslip concentrating at the southwestern end of coseismic rupture, in an area of many aftershocks and positive Coulomb failure stress change. Our findings demonstrate the power of satellite remote sensing technology in constraining source geometry and slip model of complex earthquakes when ground measurements are limited.

Introduction

The Altyn Tagh fault defines the northwestern boundary of the Tibetan plateau and contributes to the eastward extrusion of Tibet as well as the convergence between India and Eurasia (Molnar and Tapponnier, 1975; Tapponnier and Molnar, 1977; Tapponnier et al., 1982, 2001; Avouac and Tapponnier, 1993; Wittlinger et al., 1998). In northern Tibet, the Altyn Tagh fault converges with the Karakax Fault in Yutian County, where three $M_w > 6$ earthquakes occurred during 2008–2014: the 2008 M_w 7.1, the 2012 M_w 6.1, and the 2014 M_w 6.9 Yutian earthquakes. The 2008 event was related to extensional deformation (Taylor and Yin, 2009) on a nonplanar source fault, dominated by left-lateral strike slip in the north and normal faulting in the south and with a total surface rupture length of 31 km (Elliott et al., 2010; Furuya and Yasuda, 2011; Xu et al., 2013; Bie and Ryder, 2014; Song et al., 2019). The epicenter of the 2012 event was located ∼90 km to the northeast of the 2008 event and closer to the 2014 earthquake. However, this later event received less attention due to its smaller size and the paucity of satellite observations.

The 2014 M_w 6.9 Yutian earthquake occurred to the northeast of the 2012 event. It represents the third major event of the recent Yutian earthquake sequence. Similar to the two previous earthquakes, its epicenter was located close to the southwestern end of the Altyn Tagh fault where the fault splays into four main left-lateral strike-slip subfaults: the North Xor Kol, Ashikule, South Xor Kol, and Kuliya faults (Fig. 1). Li et al. (2016) used both field investigations and high-resolution optical satellite images to map the fault rupture of the 2014 event. They found that the earthquake produced a total of 25 km long rupture along two parallel left-lateral strike-slip faults as well as on a previously unidentified right-lateral strike-slip fault along the southern shoreline of Xol Kol Lake, linking the two left-lateral faults (Fig. 1). The dextral relay faulting together with the left-lateral slip on the Ashikule and South Xor Kol faults can be explained as conjugate faulting, which is widely observed across the north-central Tibetan plateau, under the present-day compressional stress field from the ongoing penetration of the Indian subcontinent into Eurasia (Li et al., 2016). The maximum sinistral displacement detected during their field investigations was found to be ∼1 m in the southern part of the piedmont of the Xor Kol basin with vertical displacements of up to ∼0.4 m.

1. Physical Science and Engineering Division, King Abdullah University of Science and Technology (KAUST), Thuwal, Saudi Arabia; 2. School of Geosciences and Info-Physics, Central South University, Changsha, China; 3. Key Laboratory of Metallogenic Prediction of Nonferrous Metals and Geological Environment Monitoring, Central South University, Changsha, China; 4. Université de Paris, Institut de Physique du Globe de Paris, CNRS, Paris, France; 5. State Key Laboratory of Earthquake Dynamics, Institute of Geology, China Earthquake Administration, Beijing, China

*Corresponding author: wenbin.xu@csu.edu.cn
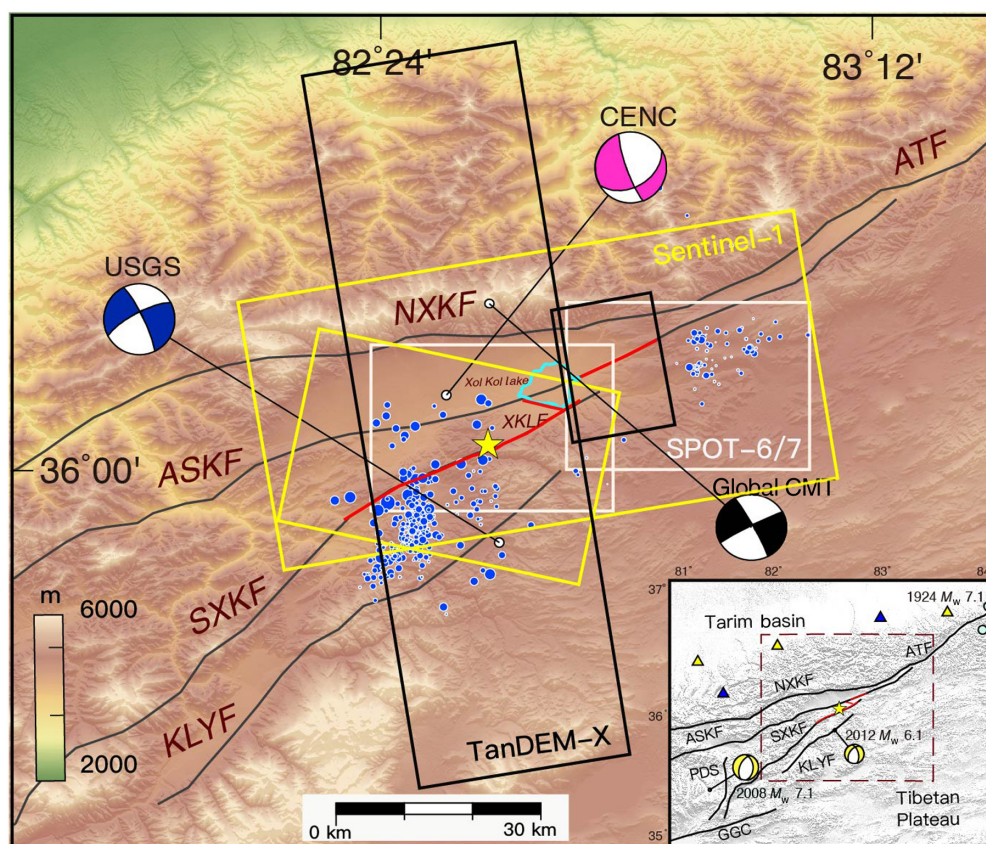
© Seismological Society of America

Figure 1. Topographic map of the 2014 M_w 6.9 Yutian earthquake (Tibet) with focal mechanism solutions determined by the U.S. Geological Survey (USGS, blue), China Earthquake Networks Center (CENC, pink), and Global Centroid Moment Tensor (Global CMT, black). Major fault traces are shown as dark gray lines, and the modeled fault segments in this study are shown in red. Rectangles represent the coverage of TanDEM-X SAR data (black), Sentinel-1 SAR data (yellow), and Satellite Pour l'Observation de la Terre (SPOT)-6/7 imagery (white). Yellow star represents the relocated epicenter (G. Zhang et al., 2014), and blue circles are relocated aftershocks (Fang et al., 2015). The inset shows the location of the study area, focal mechanisms of the 2008 M_w 7.1 and 2012 M_w 6.1 Yutian earthquakes, and locations of the two 1924 Minfeng M_w 7.1 earthquakes (light blue circles) that occurred on the Altyn Tagh fault. The yellow and blue triangles are the nearest permanent and temporal seismic stations in this region (Fang et al., 2015). ASKF, Ashikule fault; ATF, Altyn Tagh fault; GGC, Gonggacuo fault; KLYF, Kuliya fault; NXKF, North Xol Kol fault; PDS, Pingdingshan fault; SXKF, South Xor Kol fault; XKLF, Xor Kol Lake fault. The color version of this figure is available only in the electronic edition.

Because of the sparse distribution of seismic stations in this region (Fig. 1), the epicenter of the 2014 Yutian earthquake is poorly determined and details of the reported source parameters differ significantly. G. Zhang et al. (2014) used a Bayesian absolute location method to relocate the epicenter and determined it to be close to the South Xor Kol fault at 36.04° N, 82.56° E, with a depth of 12.3 km. In addition, Fang et al. (2015) used a double-difference algorithm to relocate 363 aftershocks recorded by two temporal seismic stations in addition to permanent stations; the relocated aftershocks primarily form two distinct clusters at the northeastern and southwestern ends of the ruptured fault (Fig. 1).

A few slip models have already been reported for the 2014 Yutian earthquake. Y. Zhang et al. (2014) found that the

coseismic rupture propagated predominantly toward the southwest along the South Xor Kol fault and estimated fault slip up to ~1.8 m at a depth of 20 km. Zhou et al. (2015), on the other hand, reported that the peak fault slip was shallower at ~9 km depth amounting to ~2.1 m. In another study, Zhang and Ge (2017) applied a multiarray teleseismic P-wave backprojection method to image the rupture process of the mainshock and found that the rupture propagated bilaterally along the South Xor Kol fault before jumping to the Ashikule fault. They estimated the maximum coseismic fault slip of 2.3 m at the fault conjunction area and at a depth of 5 km, from which the maximum seismic energy radiated.

The large differences between the reported fault-slip models indicate that the fault geometry and kinematics are more complex than included in previous studies (Y. Zhang et al., 2014; Zhou et al., 2015; Zhang and Ge, 2017). To better address these issues, we combine high-resolution optical and radar satellite data to generate the first coseismic and early postseismic ground deformation maps of the 2014 Yutian earthquake. We use these data to constrain the fault segment locations, geometry, and slip distribution of the event and to analyze the spatial relationship between the coseismic fault slip and early afterslip.

Coseismic Observations and Modeling
Deformation data
We used high-resolution synthetic aperture radar (SAR) data from the TanDEM-X satellite (Table 1) to generate a coseismic ground deformation map of the Yutian earthquake, acquired from two parallel ascending orbits. We processed the data with GAMMA software using a 10 m digital elevation model (DEM) to remove the effects of topography. This DEM was generated from a pair of pre-event TanDEM-X data (Table 1). The interferograms were multilooked to about 10 m and suffered significant decorrelation close to the fault ruptures because of

TABLE 1
Information about the TanDEM-X Synthetic Aperture Data (SAR) Data Used in This Study

Mode	Orbit	Incidence Angle	Master (yyyy/mm/dd)	Slave (yyyy/mm/dd)	Perpendicular Baseline (m)
Strip map	Ascending	46.19°	2012/03/25	2014/08/11	135
Strip map	Ascending	33°	2013/08/19	2014/03/27	11

large displacement gradients and steep topography near the southern half of the coseismic fault (Fig. 2c). Therefore, we used SAR-image offset tracking to compute coseismic near-fault displacements in both the range and azimuth directions (e.g., Pathier *et al.*, 2006; Wang and Jónsson, 2015). The range offsets show well the location of the surface ruptures as linear displacement discontinuities at the South Xor Kol and the Ashikule faults, which can be traced for ∼45 km (Fig. 2d). The maximum displacement across the South Xor Kol fault is found to be ∼1 m in the radar line-of-sight (LoS) direction, consistent with left-lateral fault-slip motion, whereas across the Ashikule fault it is smaller, or about 0.5 m.

In addition to the radar data analysis, we also performed sub-pixel correlation on high-resolution Satellite Pour l'Observation de la Terre (SPOT)-6/7 images (1.5 m) to generate the east–west and north–south horizontal displacement maps (Table 2). We used MicMac software to compute the multi-image subpixel correlation in the spatial domain (Michel and Avouac, 2002; Rosu *et al.*, 2015; Rupnik *et al.*, 2017). We set the size of the correlation window to be 9 × 9 pixels, which gives a better image of the fault displacement in the near-fault area (Rosu *et al.*, 2015). A map of the fault-parallel displacements D_{strike} can be generated by combining the north–south and east–west displacement fields as follows: $D_{strike} = U_e \sin\phi + U_n \cos\phi$, in which ϕ is the fault strike. The SAR image offsets and subpixel image correlation measure consistently, and both show a zone of maximum displacement along the South Xor Kol fault, although the fault-parallel displacement result suffers more artifacts due to different sun elevation and decorrelation, particularly in mountainous areas (Fig. 2a,b). Cross-correlation measurements of optical images with different sun elevation angles can lead to biased displacement determinations (Berthier *et al.*, 2005; Scherler *et al.*, 2008), whereas poor window correlation can yield inaccurate measurement values. The differences between fault-parallel displacements (from optical image offsets) and range offsets along the Ashikule fault appear to indicate a bias of the fault-parallel displacements, which might be due to different sun elevation angles of the optical images. However, the two measurements are intrinsically different with range offsets being more sensitive to vertical ground displacements.

Coseismic slip estimation

We used the SAR image range offsets, the far-field Interferometric Synthetic Aperture Data (InSAR) data, and

the east–west horizontal displacement map from the SPOT-6/7 images to estimate the spatially variable slip on the fault. Considering the smaller fault-normal displacements of strike-slip events and the relatively high noise level of the SPOT-6/7 image offsets, the observed fault-normal displacement field did not yield usable results. Similarly, due to the lower azimuth resolution of TanDEM-X SAR data, compared to the range resolution, the derived azimuth offsets were of too poor quality in this case to be useful. The coseismic datasets were first down-sampled using the quadtree algorithm (Jónsson *et al.*, 2002), and then the model set up assuming elastic dislocations in a homogeneous linear elastic half-space (Okada, 1985). From linear discontinuities in the image-offset data and the field observations by Li *et al.* (2016), we modeled three fault segments for the Yutian earthquake, that is, the South Xor Kol fault, the Ashikule fault, and the newly identified Xor Kol Lake fault. We set the depth of the modeled fault segments to 20 km, a reasonable value of the maximum fault rupture depth for many continental strike-slip earthquakes (Chen and Molnar, 1983; Lasserre *et al.*, 2005; Yang *et al.*, 2005; Chu *et al.*, 2009). The optimal dip angles were obtained from the posterior probability density function by finding the maximum a posteriori probability solution. The posterior probability density function (PDF) was calculated as follows: $p(m|d) = \frac{p(d|m)p(m)}{p(d)}$, in which $p(d|m)$ is the likelihood function of the model parameters m given data d based on residuals between the data and the model prediction of the observations, $p(m)$ expresses the prior information (in the form of a prior joint PDF) of the model parameters, and the denominator is a normalizing constant independent of m. Once the dip angles of the modeled fault segments were determined, we inverted the data for spatially variable slip (both strike- and dip slip) using Laplacian smoothening (roughness factor of 2.1 cm/km [Fig. 3c] based on an L-curve; Mendoza and Hartzell, 2013) and non-negative least squares (Wang *et al.*, 2017). The solution roughness is the average second-order finite-difference sum of each fault patch, and the unit cm/km indicates the average slip gradient. The data sets were weighted based on their variances yielding 37.4%, 62.3%, and 0.3% relative weights for the range offsets, InSAR data, and horizontal optical offsets, respectively.

Overall, the model prediction matches the observed coseismic deformation pattern well, with the largest misfits found south of the fault stepover (Fig. 2h). The root mean square
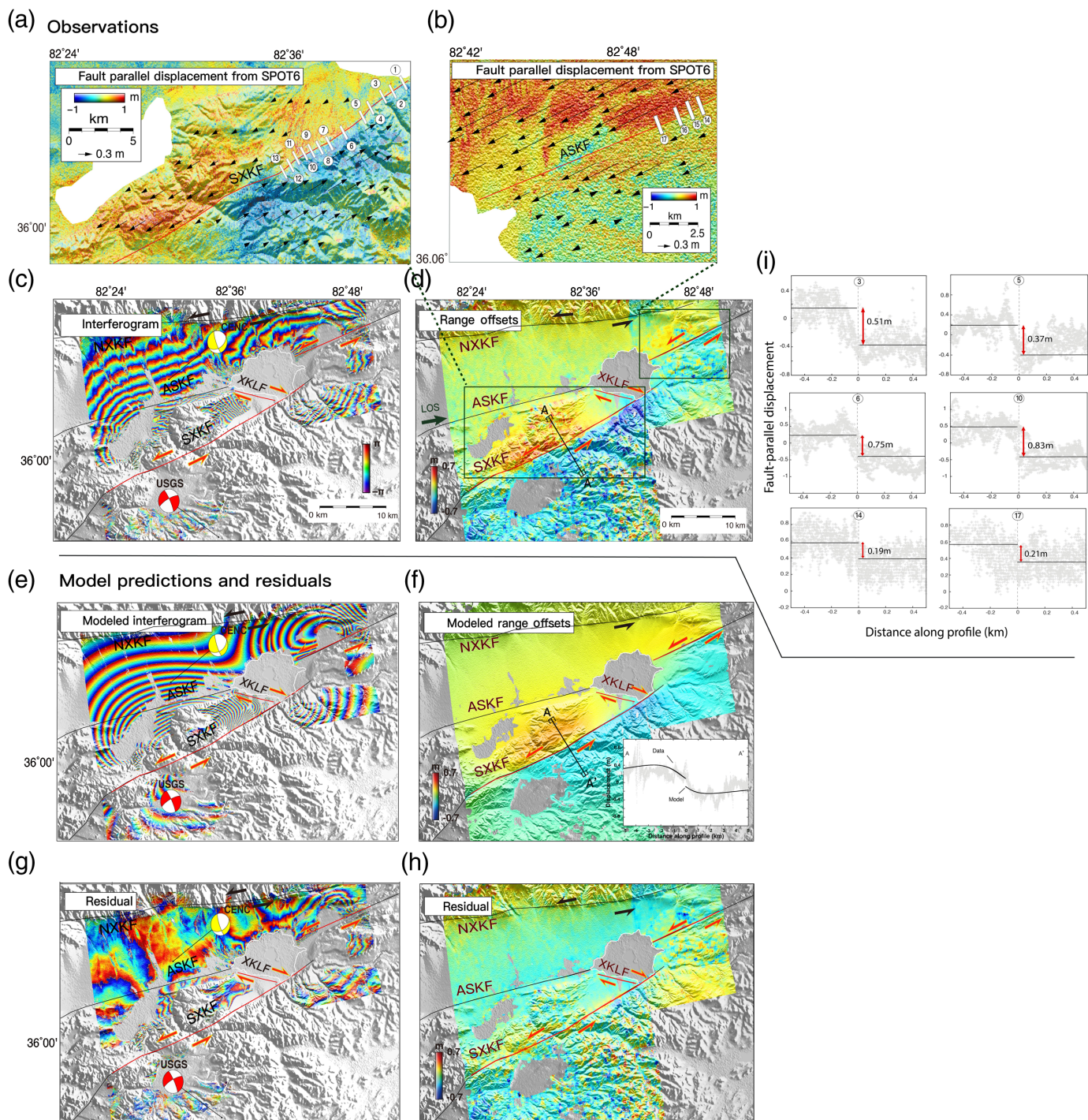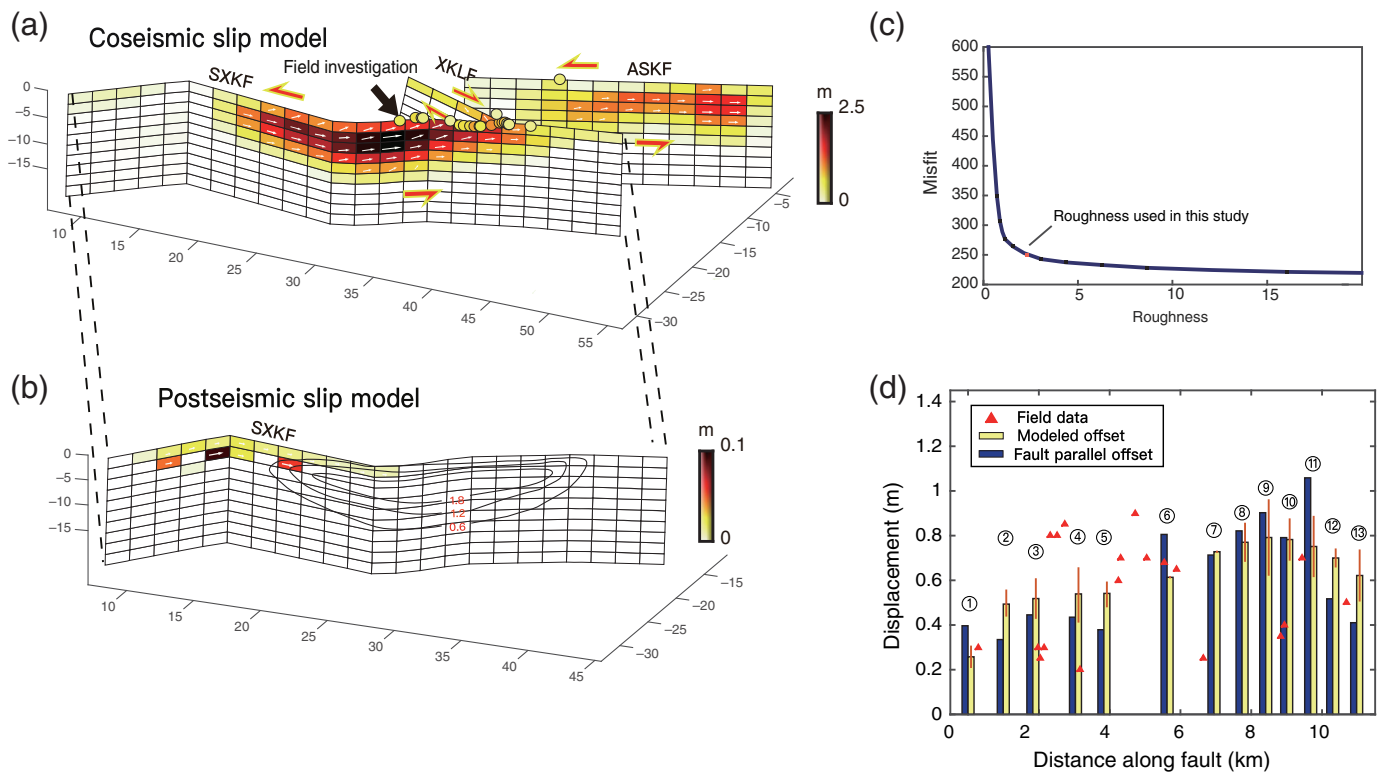
Figure 2. (a,b) Fault-parallel horizontal displacements along the SXKF and ASKF, generated from offsets between two SPOT6/7 images. (c) Observed coseismic interferogram from two neighboring pairs of TanDEM-X SAR data, with one fringe representing 1.5 cm coseismic displacement in line-of-sight (LoS). (d) Coseismic SAR image range offsets from the ascending-orbit TanDEM-X data covering the 2014 Yutian earthquake. (e) Coseismic interferogram and (f) SAR image range offsets simulated using the fault-slip model shown in Figure 3. The lower right panel in (f) shows observed (gray) and modeled (black) displacements along profile A–A′ with a width of 200 m shown in (d). (g,h) Residual between observation and prediction. (i) Fault-parallel displacements along selected across-fault profiles, with the black lines representing the median value on each side of the fault. The profile locations are shown in (a) and (b) along with other locations where the fault offset was determined and used in the comparison in Figure 3d. The red lines indicating surface fault ruptures. The color version of this figure is available only in the electronic edition.

Figure 3. (a) Coseismic and (b) postseismic slip models of the 2014 Yutian earthquake. Color-coded circles in (a) indicate the field observation results of Li *et al.* (2016). Contour lines in (b) represent the distribution of coseismic slip. Slip vector with strike slip and dip slip is plotted with slip over 0.5 m in (a), and afterslip of >1 cm is plotted in (b). (c) The L-curve between the weighted misfit of data and slip roughness, the roughness in our study is indicated by a red diamond. (d) Fault-parallel displacements from the optical image offsets and the model prediction at selected profile locations shown in Figure 2a, in comparison with the field data of Li *et al.* (2016). The color version of this figure is available only in the electronic edition.

misfit residuals are 11, 5, and 27 cm for the range offsets, InSAR data, and east–west optical-image displacements, respectively. The isolated negative residual north of the Ashikule fault is associated with an alluvial fan, whereas many small patchy residuals to the south of the South Xor Kol fault are due to the rough topography and steep slopes.

The slip model indicates that the majority of the fault slip occurred on steeply dipping faults and at depths shallower than 10 km (Fig. 3a). The modeled South Xor Kol fault and the Ashikule fault dip at $78^{+1.9°}_{-1.8°}$ and $78^{+2.7°}_{-2.8°}$ to the northwest, respectively, whereas the Xor Kol Lake fault is found to dip at $80^{+2°}_{-1.4°}$ to the southwest (Fig. S1, available in the supplemental material to this article). The South Xor Kol fault and the Ashikule fault are dominated by left-lateral strike-slip fault motion with minor normal dip slip close to the surface. On the South Xor Kol fault, the maximum left-lateral strike slip of ~2.5 m is located at 4–6 km depths close to the hypocenter and the estimated moment release is 1.1×10^{19} N · m,

accounting for 67% of the total moment release. The maximum slip of the modeled Ashikule fault reaches 1.5 m at ~4 km depth. On the Xol Kol Lake fault some shallow right-lateral slip of up to ~0.9 m is found within the top 2 km of the crust. The total geodetic moment release is estimated to be

TABLE 2
Information about the Satellite Pour l'Observation de la Terre (SPOT)-6/7 Imagery Used in This Study

Satellite	Date (yyyy/mm//dd)	Incidence Angle	Cloud	Elevation Angle
SPOT-6	2013/06/11	5.42°	0%	65.12°
SPOT-6	2013/09/30	15.92°	0%	45.92°
SPOT-7	2014/02/10	20.76°	0%	45.40°

Figure 4. (a,b) Observed and (c,d) modeled postseismic LoS deformation maps spanning from November 2014 to November 2016. Solid red line represents the fault trace of the postseismic deformation, and dashed red line represents the coseismic fault trace. Yellow star represents the relocated epicenter (G. Zhang *et al.*, 2014). The color version of this figure is available only in the electronic edition.

1.65×10^{19} N · m, corresponding to $M_w \sim 6.9$, which is somewhat lower than that estimated using seismological methods (Y. Zhang *et al.*, 2014; Zhou *et al.*, 2015). Our lower moment estimation is probably due to the fact that our data do not fully cover the entire displacement field, as can be seen from the coseismic interferogram and unresolved slip at depth due to limited far-field displacement data. To examine the data resolution for variable slip on the fault plane, we conducted a checkerboard fault-slip test, and the results show that shallow fault slip above 5 km depth is better resolved than deeper fault slip (Fig. S2).

To evaluate the reliability of estimated shallow coseismic strike slip, we compared our observed and modeled surface fault offsets with field observations by Li *et al.* (2016) at 13 locations along the South Xor Kol fault (Fig. 2a). From the fault-parallel displacement maps generated from the SPOT image data, we found a maximum offset of 1.0 ± 0.3 m located close to the maximum offset detected in the field of 0.9 m. Observations along the Ashikule fault, on the other hand, are noisy, and its displacement cannot be well quantified (Fig. 2b). In general, our geodetic observations and the modeled shallow fault slip tend to be somewhat larger than the coseismic fault offsets measured in the field (Fig. 3d). Several studies comparing geodetically determined fault offsets with field data have observed a similar tendency, for example, in the cases of the

2001 Kokoxili (Klinger *et al.*, 2005), 1999 İzmit (Çakir *et al.*, 2003), Wenchuan (Feng *et al.*, 2017), and Harrat Lunayyir (Trippanera *et al.*, 2019) earthquakes, although sometimes field observations may overestimate offsets due to difficulties in isolating the last slip event from previous earthquakes (Klinger *et al.*, 2011). The likely explanation relates to the field observations not detecting distributed deformation near the fault (Vallage *et al.*, 2015), over which the geodetic methods integrate, yielding larger values.

Postseismic Deformation Mapping and Afterslip Modeling

We also looked into the early postseismic deformation after the Yutian earthquake by processing a series of Sentinel-1 SAR images acquired from November 2014 to May 2017 from both ascending and descending orbits. The postseismic deformation

was found to be insignificant after December 2016, so we focused on data from the November 2014 to December 2016 time period. We reduced topography-dependent atmospheric signals within each interferogram by assuming a linear relationship between elevation and atmospheric delay (Doin et al., 2009; Bie et al., 2014), and we then derived the cumulative displacement map using the small baseline subset time-series approach (Berardino et al., 2002). The results show up to 3 cm of postseismic deformation in the LoS direction near the southwestern end of the South Xor Kol coseismic fault rupture in both the ascending and descending deformation maps (Fig. 4). The discontinuities in both the ascending and descending data suggest that it is a real deformation feature representing early localized postseismic surface fault creep rather than localized phase difference caused by atmospheric disturbances.

We used a similar method to estimate the postseismic slip as we did in the coseismic fault-slip modeling. Here the relative weights of the ascending and descending postseismic data are 42% and 58%, respectively. We found shallow afterslip concentrating in the uppermost ~4 km of the southwestern part of the South Xor Kol coseismic fault zone while finding no clear afterslip on the Ashikule fault (Fig. 3b). This concentration of afterslip on the South Xor Kol fault is mostly adjacent to the coseismic rupture and likely reflects both the coseismic stress increase as well as the shallow frictional properties on this part of the fault. The estimated afterslip zone also spatially correlates well with the location of one of the two groups of aftershocks that were located near the ends of coseismic slip zone. The estimated afterslip reaches up to ~0.15 m with a postseismic moment release of 1.15×10^{17} N · m, equivalent to an M_w 5.2 earthquake.

Discussion

Coseismic strike-slip ruptures are usually segmented by several fault segments, including stepovers and fault bends, which have been observed from many moderate-to-large magnitude strike-slip events (King and Nábělek, 1985; Wesnousky, 2006; Klinger et al., 2010). The 1992 M_w 7.3 Landers earthquake ruptured across three stepover zones and at least five fault segments (Sieh et al., 1993). The 2016 M_w 7.8 Kaikōura earthquake, which has one of the most complex continental earthquake ruptures, cascaded on adjacent faults into a large devastating event that ruptured at least 21 faults in the end (Hamling et al., 2017; Klinger et al., 2018; Xu et al., 2018). Our coseismic slip model of the 2014 Yutian event shows that, similarly, the South Xor Kol fault and the Ashikule fault have disconnected at the surface of ~4.5 km, but it is likely that the rupture was propagated on a linking fault, the Xor Kol Lake fault, between the two main strike-slip faults. Field investigations and experimental rupture propagation models show that the possible threshold for a rupture to jump across a stepover is about 5 km (Harris and Day, 1993, 1999; Lettis et al., 2002;

Wesnousky, 2006), and the stepover zone of the 2014 event is therefore close to this critical value. Similar rupture features were observed at the junction of two segments of the Beichuan fault of the 2008 Wenchuan earthquake (Shen et al., 2009) with slip maxima near the conjunction area.

The coseismic and postseismic deformation maps and their related slip models of the 2014 event show many common and complementary behaviors: both coseismic and postseismic deformation patterns show a consistent left-lateral strike-slip on the South Xor Kol fault. The coseismic fault-slip model reveals one major slip asperity at depths between 2 and 10 km on the South Xor Kol fault that is responsible for the major coseismic moment release. The coseismic and postseismic slips are spatially complementary, with coseismic slip concentrated close to the rough mountainous area to the northeast and postseismic slip occurring further to the southwest. The redistribution of strain energy within the surrounding area due to coseismic rupture most likely drove the afterslip (Hsu et al., 2006; Ozawa et al., 2012; Liu and Xu, 2019). No afterslip is found downdip of the coseismic rupture, which suggests a downdip extension of the velocity-weakening fault (unbroken) into the lower crust.

Earthquake activity may be promoted by an earlier earthquake when stress is increased on a fault (Stein et al., 1994; Harris, 1998). Coulomb failure stress change calculations have been performed for earthquakes to examine the correlation between aftershocks and coseismic stress changes (King et al., 1994). We used Coulomb 3.4 software (Toda et al., 2011) to model the static stress changes. The Coulomb failure stress changes calculated using the coseismic slip model show that the positive stress loading areas occur at both ends of the seismogenic faults (Fig. 5). Two clusters of aftershocks at the ends of the ruptured faults suggest that these events were triggered by coseismic stress changes. The positive Coulomb failure stress changes correlate well with the spatial distribution of aftershocks, with 78% out of 363 of aftershocks located within the areas of positive Coulomb stress changes. At a larger scale, the 2008 and 2012 earthquakes increased the Coulomb failure stress to the east of the conjunction of the Altyn Tagh fault and the Ashikule fault (Bie and Ryder, 2014) and the 2014 Yutian earthquake further increased the Coulomb failure stress on the southwestern end of the Altyn Tagh fault. However, no large magnitude earthquakes have occurred at the southwestern end of the Altyn Tagh fault since the 1924 M_w 7.1 Minfeng earthquakes (Lee et al., 2002). If we consider that the fault segment between the 1924 and 2014 events is fully locked to 10 km depth and with a deep slip rate of 7 ± 3 mm/yr (Shen et al., 2001; Li et al., 2018), the calculated moment deficit since 1924 is nearly of $2.83 \pm 1.21 \times 10^{19}$ N · m, corresponding to an M_w 6.9 earthquake. The occurrence of the 2014 event increased the seismic hazard of the fault segment between the 1924 and 2014 events.
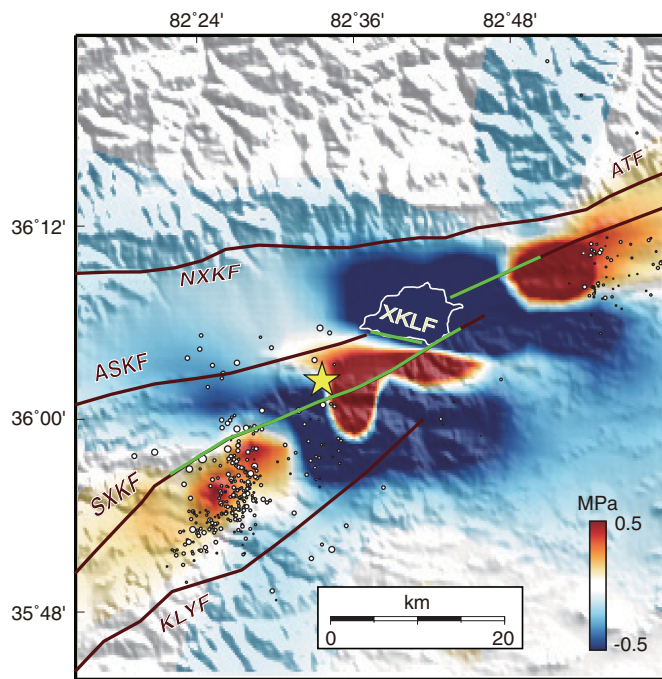
Figure 5. Spatial relationship between Coseismic Coulomb failure stress changes (ΔCFS) and aftershocks. The coseismic ΔCFS are calculated at 8 km depth, with the dip and strike angle of receiver faults at 78° and 235°, respectively. Green solid lines represent the surface trace of the modeled faults, and the yellow star represents the relocated epicenter (G. Zhang *et al.*, 2014). The color version of this figure is available only in the electronic edition.

Conclusions

In this study, we presented the first coseismic and postseismic deformation maps associated with the 2014 Yutian M_w 6.9 earthquake. We found that three faults ruptured during the event and that the rupture jumped from the South Xor Kol fault to the Ashikule fault with a stepover of 4.5 km across Xol Kol Lake. The interactions between strike-slip faults and the extensional stepover zone and different focal mechanisms of recent large earthquakes reflect the complex tectonic environment at the southwestern end of the Altyn Tagh fault on the eastern Tibetan plateau. Using a joint inversion of coseismic interferograms, high-resolution radar, and optical image-offset measurements, we estimated that shallow fault slip on steep faults occurred in the 2014 Yutian earthquake, with a maximum of 2.5 m of left-lateral fault slip located at 6 km depth on the South Xor Kol fault. The coseismic moment release was estimated to be 1.65×10^{19} N · m, corresponding to $M_w \sim 6.8$. We generated the postseismic deformation maps using nearly 2 yr of postseismic InSAR time series data, used the maps to invert for afterslip, and found that up to ~3 cm of afterslip occurred close to the surface. The afterslip mainly occurred near the southwestern end of the coseismic rupture where Coulomb failure stress changes were found to be strongly positive and

many aftershocks took place. Considering the complex seismotectonics as well as historical and recent earthquakes in the region, we suggest that special attention should be paid to the southwestern segment of the Altyn Tagh fault and the vicinity of the 2014 Yutian earthquake.

Data and Resources

The relocated aftershocks were provided by L. Fang (doi: 10.6038/cjg20150310). Sentinel-1 synthetic aperture radar (SAR) images were downloaded from the Sentinel Data Hub (https://scihub.copernicus.eu, last accessed November 2016). The moment tensor solutions were from the U.S. Geological Survey (USGS; http://earthquake.usgs.gov, last accessed June 2017), the Global Centroid Moment Tensor project (CMT; http://www.globalcmt.org, last accessed June 2017), and the China Earthquake Networks Center (CENC; http://data.earthquake.cn/index.html, last accessed June 2017). The TanDEM-X SAR images were provided by German Aerospace Centre (DLR) through project XTI_GEOL3441. Several figures were prepared using Generic Mapping Tools software. The co- and postseismic fault-slip models in this study are available at https://github.com/Wenbin16/2014Yutian-Eq (last accessed July 2020). The supplemental material for this article includes the checkerboard test and posterior distribution of dip angles of the modeled faults.

Acknowledgments

References

Avouac, J. P., and P. Tapponnier (1993). Kinematic model of active deformation in Central Asia, *Geophys. Res. Lett.* **20,** no. 10, 895–898.

Berardino, P., G. Fornaro, R. Lanari, and E. Sansosti (2002). A new algorithm for surface deformation monitoring based on small baseline differential SAR interferograms, *IEEE Trans. Geosci. Rem. Sens.* **40,** no. 11, 2375–2383, doi: 10.1109/TGRS.2002.803792.

Berthier, E., H. Vadon, D. Baratoux, Y. Arnaud, C. Vincent, K. L. Feigl, F. Remy, and B. Legresy (2005). Surface motion of mountain glaciers derived from satellite optical imagery, *Rem. Sens. Environ.* **95,** 14–28, doi: 10.1016/j.rse.2004.11.005.

Bie, L., and I. Ryder (2014). Recent seismic and aseismic activity in the Ashikule stepover zone, NW Tibet, *Geophys. J. Int.* **198,** no. 3, 1632–1643, doi: 10.1093/gji/ggu230.

Bie, L., I. Ryder, S. E. Nippress, and R. Bürgmann (2014). Coseismic and post-seismic activity associated with the 2008 Mw 6.3

Damxung earthquake, Tibet, constrained by InSAR, *Geophys. J. Int.* **196,** no. 2, 788–803, doi: 10.1093/gji/ggt444.

Çakir, Z., J. B. D. Chabalier, R. Armijo, B. Meyer, A. Barka, and G. Peltzer (2003). Coseismic and early post-seismic slip associated with the 1999 Izmit earthquake (Turkey), from SAR interferometry and tectonic field observations, *Geophys. J. Int.* **155,** no. 1, 93–110, doi: 10.1046/j.1365-246X.2003.02001.x.

Chen, W. P., and P. Molnar (1983). Focal depths of intracontinental and intraplate earthquakes and their implications for the thermal and mechanical properties of the lithosphere, *J. Geophys. Res.* **88,** no. B5, 4183–4214, doi: 10.1029/JB088iB05p04183.

Chu, R., L. Zhu, and D. V. Helmberger (2009). Determination of earthquake focal depths and source time functions in central Asia using teleseismic P waveforms, *Geophys. Res. Lett.* **36,** no. 17, doi: 10.1029/2009GL039494.

Doin, M. P., C. Lasserre, G. Peltzer, O. Cavalie, and C. Doubre (2009). Corrections of stratified tropospheric delays in SAR interferometry: Validation with global atmospheric models, *J. Appl. Geophys.* **69,** no. 1, 35–50, doi: 10.1016/j.jappgeo.2009.03.010.

Elliott, J. R., R. J. Walters, P. C. England, J. A. Jackson, Z. Li, and B. Parsons (2010). Extension on the Tibetan plateau: Recent normal faulting measured by InSAR and body wave seismology, *Geophys. J. Int.* **183,** no. 2, 503–535, doi: 10.1111/j.1365-246X.2010.04754.x.

Fang, L. H., J. P. Wu, W. L. Wang, T. Yang, and C. Z. Wang (2015). Relocation of the 2014 Ms 7.3 earthquake sequence in Yutian, Xinjiang, *China J. Geophys.* **58,** no. 3, doi: 10.1098/rspb.2009.1465.

Feng, G., S. Jónsson, and Y. Klinger (2017). Which fault segments ruptured in the 2008 Wenchuan earthquake and which did not? New evidence from near-fault 3D surface displacements derived from SAR image offsets, *Bull. Seismol. Soc. Am.* **107,** 1185–1200, doi: 10.1785/0120160126.

Furuya, M., and T. Yasuda (2011). The 2008 Yutian normal faulting earthquake (Mw 7.1), NW Tibet: Non-planar fault modeling and implications for the Karakax Fault, *Tectonophysics* **511,** nos. 3/4, 125–133, doi: 10.1016/j.tecto.2011.09.003.

Hamling, I. J., S. Hreinsdóttir, K. Clark, J. Elliott, C. Liang, E. Fielding, N. Litchfield, P. Villamor, L. Wallace, T. J. Wright, *et al.* (2017). Complex multifault rupture during the 2016 Mw 7.8 Kaikōura earthquake, New Zealand, *Science* **356,** no. 6334, eaam7194 , doi: 10.1126/science.aam7194.

Harris, R. A. (1998). Introduction to special section: Stress triggers, stress shadows, and implications for seismic hazard, *J. Geophys. Res.* **103,** no. B10, 24,347–24,358, doi: 10.1029/98JB01576.

Harris, R. A., and S. M. Day (1993). Dynamics of fault interaction: Parallel strike-slip faults, *J. Geophys. Res.* **98,** no. B3, 4461–4472, doi: 10.1029/92JB02272.

Harris, R. A., and S. M. Day (1999). Dynamic 3D simulations of earthquakes on en echelon faults, *Geophys. Res. Lett.* **26,** no. 14, 2089–2092, doi: 10.1029/1999GL900377.

Hsu, Y. J., M. Simons, J. P. Avouac, J. Galetzka, K. Sieh, M. Chlieh, D. Natawidjaja, L. Prawirodirdjo, and Y. Bock (2006). Frictional afterslip following the 2005 Nias-Simeulue earthquake, Sumatra, *Science* **312,** no. 5782, 1921–1926, doi: 10.1126/science.1126960.

Jónsson, S., H. Zebker, P. Segall, and F. Amelung (2002). Fault slip distribution of the 1999 Mw 7.1 Hector Mine, California, earthquake, estimated from satellite radar and GPS measurements, *Bull. Seismol. Soc. Am.* **92,** no. 4, 1377–1389, doi: 10.1785/0120000922.

King, G., and J. Nábělek (1985). Role of fault bends in the initiation and termination of earthquake rupture, *Science* **228,** no. 4702 (1985), 984–987, doi: 10.1126/science.228.4702.984.

King, G. C., R. S. Stein, and J. Lin (1994). Static stress changes and the triggering of earthquakes, *Bull. Seismol. Soc. Am.* **84,** no. 3, 935–953.

Klinger, Y. (2010). Relation between continental strike-slip earthquake segmentation and thickness of the crust, *J. Geophys. Res.* **115,** no. B7, doi: 10.1029/2009JB006550.

Klinger, Y., M. Etchebes, P. Tapponnier, and C. Narteau (2011). Characteristic slip for five great earthquakes along the FuYun fault in China, *Nat. Geosci.* **4,** no. 6, 389–392, doi: 10.1038/ngeo1158.

Klinger, Y., K. Okubo, A. Vallage, J. Champenois, A. Delorme, E. Rougier, Z. Lei, E. E. Knight, A. Munjiza, C. Satriano, *et al.* (2018). Earthquake damage patterns resolve complex rupture processes, *Geophys. Res. Lett.* **45,** no. 19, 10–279, doi: 10.1029/2018GL078842.

Klinger, Y., X. Xu, P. Tapponnier, J. Van der Woerd, C. Lasserre, and G. King (2005). High-resolution satellite imagery mapping of the surface rupture and slip distribution of the Mw ∼ 7.8, 14 November 2001 Kokoxili earthquake, Kunlun fault, northern Tibet, China, *Bull. Seismol. Soc. Am.* **95,** no. 5, 1970–1987, doi: 10.1785/0120040233.

Lasserre, C., G. Peltzer, F. Crampé, Y. Klinger, J. Van Der Woerd, and P. Tapponnier (2005). Coseismic deformation of the 2001 Mw= 7.8 Kokoxili earthquake in Tibet, measured by synthetic aperture radar interferometry, *J. Geophys. Res.* **110,** no. B12, doi: 10.1029/2004JB003500.

Lee, W. H., P. Jennings, C. Kisslinger, and H. Kanamori (Editors) (2002). *International Handbook of Earthquake & Engineering Seismology*, Part A, Elsevier, London, United Kingdom.

Lettis, W., J. Bachhuber, R. Witter, C. Brankman, C. E. Randolph, A. Barka, W. D. Page, and A. Kaya (2002). Influence of releasing stepovers on surface fault rupture and fault segmentation: Examples from the 17 August 1999 Izmit earthquake on the North Anatolian fault, Turkey, *Bull. Seismol. Soc. Am.* **92,** no. 1, 19–42, doi: 10.1785/0120000808.

Li, H., J. Pan, A. Lin, Z. Sun, D. Liu, J. Zhang, C. Li, K. Liu, M. L. Chevalier, K. Yun, *et al.* (2016). Coseismic surface ruptures associated with the 2014 Mw 6.9 Yutian earthquake on the Altyn Tagh fault, Tibetan plateau, *Bull. Seismol. Soc. Am.* **106,** no. 2, 595–608, doi: 10.1785/0120150136.

Li, Y., X. Shan, C. Qu, Y. Liu, and N. Han (2018). Crustal deformation of the Altyn Tagh Fault based on GPS, *J. Geophys. Res.* **123,** no. 11, 10,309–10,322, doi: 10.1029/2018JB015814.

Liu, X., and W. Xu (2019). Logarithmic model joint inversion method for coseismic and postseismic slip: Application to the 2017 Mw 7.3 Sarpol Zahāb earthquake, Iran, *J. Geophys. Res.* **124,** 12,034–12,052, doi: 10.1029/2019JB017953.

Mendoza, C., and S. Hartzell (2013). Finite-fault source inversion using teleseismic P waves: Simple parameterization and rapid analysis, *Bull. Seismol. Soc. Am.* **103,** no. 2A, 834–844, doi: 10.1785/0120120069.

Michel, R., and J. P. Avouac (2002). Deformation due to the 17 August 1999 Izmit, Turkey, earthquake measured from SPOT images, *J. Geophys. Res.* **107,** no. B4, ETG-2 , doi: 10.1029/2000JB000102.

Molnar, P., and P. Tapponnier (1975). Cenozoic tectonics of Asia: effects of a continental collision, *Science* **189,** no. 4201, 419–426, doi: 10.1126/science.189.4201.419.

Okada, Y. (1985). Surface deformation due to shear and tensile faults in a half-space, *Bull. Seismol. Soc. Am.* **75,** no. 4, 1135–1154.

Ozawa, S., T. Nishimura, H. Munekane, H. Suito, T. Kobayashi, M. Tobita, and T. Imakiire (2012). Preceding, coseismic, and postseismic slips of the 2011 Tohoku earthquake, Japan, *J. Geophys. Res.* **117,** no. B7 (2012), doi: 10.1029/2011JB009120.

Pathier, E., E. J. Fielding, T. J. Wright, R. Walker, B. E. Parsons, and S. Hensley (2006). Displacement field and slip distribution of the 2005 Kashmir earthquake from SAR imagery, *Geophys. Res. Lett.* **33,** no. 20, doi: 10.1029/2006GL027193.

Rosu, A. M., M. Pierrot-Deseilligny, A. Delorme, R. Binet, and Y. Klinger (2015). Measurement of ground displacement from optical satellite image correlation using the free open-source software MicMac, *ISPRS J. Photogram. Rem. Sens.* **100,** 48–59, doi: 10.1016/j.isprsjprs.2014.03.002.

Rupnik, E., M. Daakir, and M. P. Deseilligny (2017). MicMac—A free, open-source solution for photogrammetry, *Open Geospatial Data Software Stand.* **2,** no. 1, 14, doi: 10.1186/s40965-017-0027-2.

Scherler, D., S. Leprince, and M. R. Strecker (2008). Glacier-surface velocities in alpine. terrain from optical satellite imagery—Accuracy improvement and quality assessment, *Rem. Sens. Environ.* **112,** no. 10, 3806–3819, doi: 10.1016/j.rse.2008.05.018.

Shen, Z. K., J. Sun, P. Zhang, Y. Wan, M. Wang, R. Bürgmann, Y. Zeng, W. Gan, H. Liao, and Q. Wang (2009). Slip maxima at fault junctions and rupturing of barriers during the 2008 Wenchuan earthquake, *Nature Geosci.* **2,** no. 10, 718, doi: 10.1038/ngeo636.

Shen, Z. K., M. Wang, Y. Li, D. D. Jackson, A. Yin, D. Dong, and P. Fang (2001). Crustal deformation along the Altyn Tagh fault system, western China, from GPS, *J. Geophys. Res.* **106,** no. B12, 30,607–30,621, doi: 10.1029/2001JB000349.

Sieh, K., L. Jones, E. Hauksson, K. Hudnut, D. Eberhart-Phillips, T. Heaton, S. Hough, K. Hutton, H. Kanamori, A. Lilje, *et al.* (1993). Near-field investigations of the Landers earthquake sequence, April to July 1992, *Science* **260,** no. 5105, 171–176, doi:10.1126/science.260.5105.171.

Song, X., N. Han, X. Shan, C. Wang, Y. Zhang, H. Yin, G. Zhang, and W. Xiu (2019). Three-dimensional fault geometry and kinematics of the 2008 Mw 7.1 Yutian earthquake revealed by very-high resolution satellite stereo imagery, *Rem. Sens. Environ.* **232,** 111,300, doi: 10.1016/j.rse.2019.111300.

Stein, R. S., G. C. King, and J. Lin (1994). Stress triggering of the 1994 M= 6.7 Northridge, California, earthquake by its predecessors, *Science* **265,** no. 5177, 1432–1435, doi: 10.1126/science.265.5177.1432.

Tapponnier, P., and P. Molnar (1977). Active faulting and tectonics in China, *J. Geophys. Res.* **82,** no. 20, 2905–2930.

Tapponnier, P., G. Peltzer, A. Y. Le Dain, R. Armijo, and P. Cobbold (1982). Propagating extrusion tectonics in Asia: New insights from simple experiments with plasticine, *Geology* **10,** no. 12, 611–616, doi: 10.1130/00917613(1982)10<611:PETIAN>2.0.CO;2.

Tapponnier, P., X. Zhiqin, F. Roger, B. Meyer, N. Arnaud, G. Wittlinger, and Y. Jingsui (2001). Oblique stepwise rise and growth of the Tibet plateau, *Science* **294,** no. 5547, 1671–1677, doi:10.1126/science.105978.

Taylor, M., and A. Yin (2009). Active structures of the Himalayan-Tibetan orogen and their relationships to earthquake distribution, contemporary strain field, and Cenozoic volcanism, *Geosphere* **5,** no. 3, 199–214, doi: 10.1130/GES00217.1.

Toda, S., R. S. Stein, V. Sevilgen, and J. Lin (2011). *Coulomb 3.3 graphic-rich deformation and stress-change software for earthquake, tectonic, and volcano research and teaching-user guide*, *U.S. Geol. Surv. Open-File Rept. 1060*, p. 63.

Trippanera, D., J. Ruch, L. Passone, and S. Jónsson (2019). Structural mapping of dike-induced faulting in Harrat Lunayyir (Saudi Arabia) by using high resolution drone imagery, *Front. Earth Sci.* **7,** 168, doi: 10.3389/feart.2019.00168.

Vallage, A., Y. Klinger, R. Grandin, H. S. Bhat, and M. Pierrot-Deseillign (2015). Inelastic surface deformation during the 2013 Mw 7.7 Balochistan, Pakistan, earthquake, *Geology*, doi: 10.1130/G37290.1.

Wang, S., C. Xu, Y. Wen, Z. Yin, G. Jiang, and L. Fang (2017). Slip model for the 25 November 2016 Mw 6.6 Aketao earthquake, western China, revealed by Sentinel-1 and ALOS-2 observations, *Rem. Sens.* **9,** no. 4, 325, doi: 10.3390/rs9040325.

Wang, T., and S. Jónsson (2015). Improved SAR amplitude image offset measurements for deriving three-dimensional coseismic displacements, *IEEE J. Sel. Top. Appl. Earth Obs. Rem. Sens.* **8,** no. 7, 3271–3278, doi: 10.1109/jstars.2014.2387865.

Wesnousky, S. G. (2006). Predicting the endpoints of earthquake ruptures, *Nature* **444,** no. 7117, 358, doi: 10.1038/nature05275.

Wittlinger, G., P. Tapponnier, G. Poupinet, J. Mei, S. Danian, G. Herquel, and F. Masson (1998). Tomographic evidence for localized lithospheric shear along the Altyn Tagh fault, *Science* **282,** no. 5386, 74–76, doi: 10.1126/science.282.5386.74.

Xu, W., G. Feng, L. Meng, A. Zhang, J. P. Ampuero, R. Burgmann, and L. Fang (2018). Transpressional rupture cascade of the 2016 Mw 7.8 Kaikoura earthquake, New Zealand, *J. Geophys. Res.* **123,** doi: 10.1002/2017JB015168.

Xu, X., X. Tan, G. Yu, G. Wu, W. Fang, J. Chen, H. Song, and J. Shen (2013). Normal-and oblique-slip of the 2008 Yutian earthquake: Evidence for eastward block motion, northern Tibetan plateau, *Tectonophysics* **584,** 152–165, doi: 10.1016/j.tecto.2012.08.007.

Yang, Z. X., F. Waldhauser, Y. T. Chen, and P. G. Richards (2005). Double-difference relocation of earthquakes in central-western China, 1992–1999, *J. Seismol.* **9,** no. 2, 241–264, doi: 10.1007/s10950-005-3988-z.

Zhang, G., J. Lei, and C. Sun (2014). Relocation of the 12 February 2014 Yutian, Xiangjiang, mainshock (Ms 7.3) and its aftershock sequence, *China J. Geophys.* **57,** no. 3, 1012–1020, doi: 10.6038/cjg20140330.

Zhang, H., and Z. Ge (2017). Stepover Rupture of the 2014 M w 7.0 Yutian, Xinjiang, Earthquake, *Bull. Seismol. Soc. Am.* **107,** no. 2, 581–591, doi:10.1785/0120160099.

Zhang, Y., L. Xu, Y. Chen, and R. Wang (2014). Fast inversion for the rupture process of the 12 February 2014 Yutian Mw 6.9 earthquake: Discussion on the impacts of focal mechanisms on rupture process inversions, *Acta Seismol. Sin.* **36,** no. 2, 159–164, doi: 10.3969/j.issn.0253-3782.2014.02.001.

Zhou, Y., W. Wang, L. Xiong, and J. He (2015). Rupture process of 12 February 2014, Yutian Mw 6.9 earthquake and stress change on nearby faults, *Chin J. Geophys.* **58,** no. 1, 184–193, doi: 10.6038/cjg20150116.